Hydrogen Storage Properties of Magnesium Diboride Nanosheets Synthesized via Mechanochemical Exfoliation

Harini Gunda,[2,3] Keith G. Ray,[4] Leonard E. Klebanoff,[†] Chaochao Dun,[5] Maxwell A. T. Marple,[§] Sichi Li,[§] Peter Sharma,[6] Raymond W. Friddle,[†] Joshua D. Sugar,[†] Jonathan L. Snider,[†] Robert D. Horton,[†] Brendan C. Davis,[†] Jeffery M. Chames,[†] Yi-Sheng Liu,[7] Jinghua Guo,[‡‡] Harris E. Mason,[§] Jeffrey J. Urban,[**] Brandon C. Wood,[§] Mark D. Allendorf,[†] Kabeer Jasuja,[‡,*] Vitalie Stavila,[†,*]

Abstract

Metal boride nanostructures have shown significant promise for hydrogen storage applications. However, the synthesis of nanoscale metal-boride particles is challenging because of their high surface energy, strong inter- and intra-planar bonding, and difficult-to-control surface termination. Here, we demonstrate that mechanochemical exfoliation of magnesium diboride in zirconia produces 3-4 nm ultra-thin MgB_2 nanosheets in high yield. High-pressure hydrogenation of these nanosheets at 70 MPa and 330 °C followed by dehydrogenation at 390 °C revealed a hydrogen capacity of 5.1 wt.%, which is ~50 times larger than the capacity of bulk MgB_2 under the same conditions. This enhancement is attributed to the creation of defective sites by ball-milling and incomplete Mg surface coverage in nanosheets, which disrupts the stable boron-boron ring structure. Our DFT calculations indicate that the balance of Mg on the MgB_2 nanosheet surface changes as the material hydrogenates, as it is energetically favorable to trade a small number of Mg vacancies in $Mg(BH_4)_2$ for greater Mg coverage on the MgB_2 surface. The exfoliation and creation of ultrathin layers is a promising new direction for 2D metal boride/borohydride research with the potential to achieve high-capacity reversible hydrogen storage at more moderate pressures and temperatures.

[2] Sandia National Laboratories, 7011 East Ave, Livermore, CA, 94550, USA
[3] Indian Institute of Technology Gandhinagar, Palaj, Gandhinagar, Gujarat, 382355, India
[4] Lawrence Livermore National Laboratory, 7000 East Ave, Livermore, CA, 94550, USA
[5] The Molecular Foundry, Lawrence Berkeley National Laboratory, Berkeley, CA, 94720, USA
[6] Sandia National Laboratories, 1515 Eubank SE, Albuquerque, NM, 87185, USA
[7] The Advanced Light Source, Lawrence Berkeley National Laboratory, Berkeley, CA, 94720, USA
E-mail: kabeer@iitgn.ac.in; vnstavi@sandia.gov

1. Introduction

Today, there is a critical need for sustainable carbon-free energy storage technologies that can address the intermittent and "non-dispatchable" character of renewable energy resources.[1] Hydrogen-based technologies satisfy such requirements and are attainable long-term solutions with a potential for zero-carbon emissions.[2] Thus, hydrogen has the highest gravimetric energy density of any fuel (121 MJ/kg),[3] and is considered a viable solution for ground transportation, aircraft, and marine vessels.[3,4] At the same time, hydrogen is outperformed by hydrocarbon fuels in terms of volumetric energy density, motivating the development of advanced materials-based storage methods.[5] Compared to high-pressure H_2 storage, solid-state storage technology offers potential safety advantages (due to low pressure operation), with the additional benefit of higher volumetric density.[6] Materials considered for reversible H_2 storage include interstitial metal hydrides,[7] complex metal hydrides,[8] metal-organic frameworks (MOFs),[9] and various nanomaterials.[10] Metal hydrides are among the lead candidate materials for mobile applications, as they display high volumetric densities;[10,12,13] however, the enthalpy ΔH required to release H_2 is typically too high, which translates to dehydriding temperatures that are impractical.

Nanostructuring is an important strategy to improve both the thermodynamics and kinetics of metal hydrides[12,13] by offering enhanced surface area and altered nanointerfaces.[10, 14-16] The enhanced hydrogen storage and improved kinetics of hydrogen uptake and release in nanomaterials are largely due to the creation of additional binding sites (reactive planes, edges, corners, and lattice defects) that accelerate mass transport and intermolecular reactions.[17-19] A number of reports describe the properties of nanostructured hydrides (e.g., MgH_2, $Mg(BH_4)_2$, Pd, Li_2NH)[32-35] and nanoconfined hydrides on various supports (e.g., MgH_2@MOF, MgH_2@graphene, MgH_2@carbon, $NaAlH_4$@SBA-15, $LiNH_2$@carbon),[36-40] with improved reversibility and enhanced kinetics, highlighting their potential for reversible hydrogen storage applications.

Lightweight metal borohydrides such as $LiBH_4$, $NaBH_4$, $Mg(BH_4)_2$, and $Ca(BH_4)_2$ display both high gravimetric and volumetric hydrogen capacities.[8,41] In particular, magnesium borohydride ($Mg(BH_4)_2$) has a theoretical gravimetric hydrogen storage capacity of 14.9 wt.% H_2, coupled with favorable thermodynamic properties that lie close to the viability window of the DOE's targets.[42,43] The dehydrogenation pathway of $Mg(BH_4)_2$ has received significant attention, with several decomposition pathways identified.[44-53] The direct hydrogenation of MgB_2 to $Mg(BH_4)_2$ was successfully accomplished in studies by Severa *et al*.,[54] Pistidda *et al*.,[55] and Newhouse *et al*.,[56] and reveals the hydrogenation reaction of bulk MgB_2 requires very high hydrogen pressures (~ 90-100 MPa), high temperatures (~ 390-400 °C) and takes many hours for completion. Li *et al*. have reported the hydrogenation and dehydrogenation of nanoscale MgB_2 produced by mechanical milling, although the exact reaction pathway and the nature of intermediates formed are unclear.[57] The reaction pathway seems to be sensitive to hydrogenation conditions and particle geometry, which highlights the need to understand and improve the hydrogenation kinetics of MgB_2 to realize its full potential for hydrogen storage.

Ray *et al*.[43] investigated the initial hydrogenation of MgB_2 by a joint experimental/theoretical approach to probe the reaction mechanism. It was found that strained B–B bonds at grain boundaries or lattice point defects play an important role in the hydrogenation of MgB_2. These findings suggest that nanoscaling MgB_2 could create a high density of strained B–B bonds with enhanced reactivity towards hydrogen. With this perspective, Liu et al.[58] demonstrated improved hydrogen storage properties of a nanoscale Mg-B material made by surfactant-assisted ball milling of MgB_2. Using surfactants resulted in a surface-functionalized form of nanoscale Mg-B. Some of us previously demonstrated successful exfoliation of MgB_2 by various liquid-phase[59-65] and solid-state synthesis routes.[66] The liquid-phase exfoliation routes of MgB_2 have resulted in chemically modified boron-rich nanosheets.[59] Such nanosheets can be directly hydrogenated, but the surface decoration complicates the hydrogenation process. Hence, new approaches are needed to achieve a high degree of delamination of MgB_2 layers in pristine form.

Here, we probe the exfoliation of MgB_2 into 2D nanosheets without any associated surface functionalization by using high-energy ball milling (HEBM). Our main hypothesis was that

exfoliation of layered MgB_2 into nanosheets might significantly affect the delocalized π bonding in the graphite-like boron layers, leading to a destabilization of the B-B honeycomb structure. This in turn could lead to improved kinetics of the hydrogen uptake reaction, thereby enabling full hydrogenation into $Mg(BH_4)_2$ under milder conditions of hydrogen pressure and temperature. This solvent-free HEBM exfoliation synthetic approach yields ultra-thin MgB_2 nanosheets with a thickness of ~3-4 nm. The MgB_2 nanosheets obtained under optimized milling time display a remarkable enhancement in hydrogenation of MgB_2 into $Mg(BH_4)_2$ with a capacity of ~5.1 wt.% H_2 on the first cycle, which is ~50 times higher than the observed hydrogenation/dehydrogenation capacity of bulk MgB_2 under the same conditions of T (330 °C) and P (70 MPa H_2).

2. Results and Discussion

The mechanochemically-driven exfoliation of layered MgB_2 with isolation of ultra-thin nanosheets is shown in Supporting Information (SI) Figure S1 and involves . Figure 1(a) presents XRD analysis of the milled powders obtained at t_{BM} of 1, 2, 4, and 16 hours. As milling time increases, a significant XRD peak broadening is observed, suggesting that HEBM was efficient in reducing the crystallite size in MgB_2.[73] Figure 1(b) shows that the (001) peak, corresponding to the direction perpendicular to the B-B planes, broadens with an increase in milling time and almost vanishes with 4 h of milling, indicating a high degree of exfoliation. However, upon increasing the milling time to 16 h, the (001) peak reappears, indicating the restacking of the layers in the c-direction. This could be due to the known phenomenon of sintering that occurs with extensive milling.[74-78] The high-intensity (101) peak of MgB_2 at ~42.5º gradually broadens with milling time, suggesting a decrease in crystallite size and increase in lattice disorder/defects. A slight shift of the (101) peak to lower angle in the 16 hours milled sample was also observed, indicating an increase in d-spacing between the planes.

To quantify the effect of HEBM on the crystallite size of MgB_2, we measured the full width half maximum (FWHM) of the (101) peak for various milling times. As shown in Figure 1(c),

the FWHM of the (101) peak increases from 0.52° for bulk MgB_2, to 2.39° for 16 h milling. As the change in FWHM values from 4 h to 16 h of milling was comparatively low, we consider the optimal milling time as 4 h. Using Scherrer's formula,[67] we found that the crystallite size for the 4 h milled MgB_2 is ~4 nm. Therefore, from the XRD analysis, it was evident that HEBM can significantly reduce the crystallite size of MgB_2, increase the d-spacing between lattice planes, suggesting that exfoliation of MgB_2 does occur under these conditions.

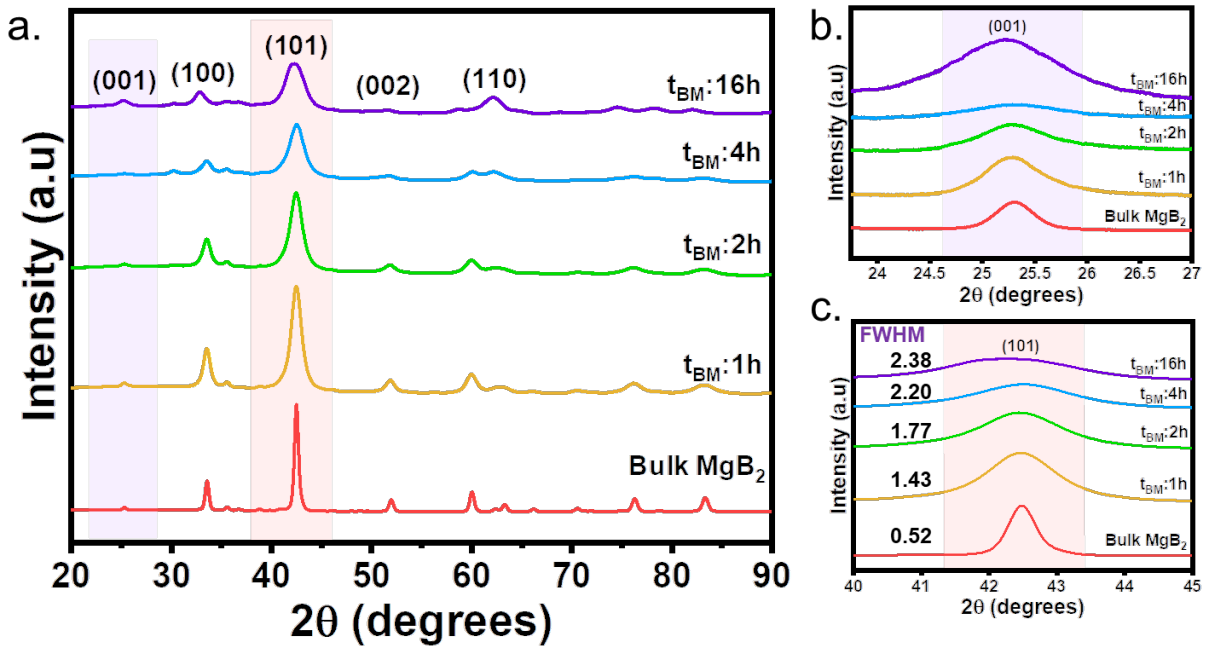

Figure 1. XRD analysis: (a) comparison of XRD data of bulk MgB_2 with the exfoliated MgB_2 obtained by high energy ball milling at various milling times (t_{BM}: 1 h, 2 h, 4 h, and 16 h); (b) comparing (001) XRD peaks of exfoliated MgB_2 at various t_{BM} with bulk MgB_2; (c) comparing (101) peaks of exfoliated MgB_2 at various t_{BM} with bulk MgB_2, with the FWHM of the (101) peak listed in degrees 2θ.

The degree of exfoliation of the 4 h ball milled MgB_2 sample was probed using AFM, TEM/ HR-TEM, and FE-SEM imaging. The AFM images shown in Figure 2(a) and 2(b), as well as the sample height analyses shown in Figure 2(c) and Figure 2(d) indicate the nanosheets have average thicknesses of ~3 to 4 nm (additional AFM 2D scans and height profiles are shown in SI as Figure S2). This confirms that solvent-free mechanical exfoliation of MgB_2 can be achieved

using HEBM with zirconia to produce ultra-thin MgB_2 nanosheets. We note here that several prior studies of the MgB_2 system either used no ball milling[43] or 1- 2 hours of ball milling with tungsten carbide vessel and balls,[79-81] with significant improvements observed in reactivity with hydrogen of ball-milled products.

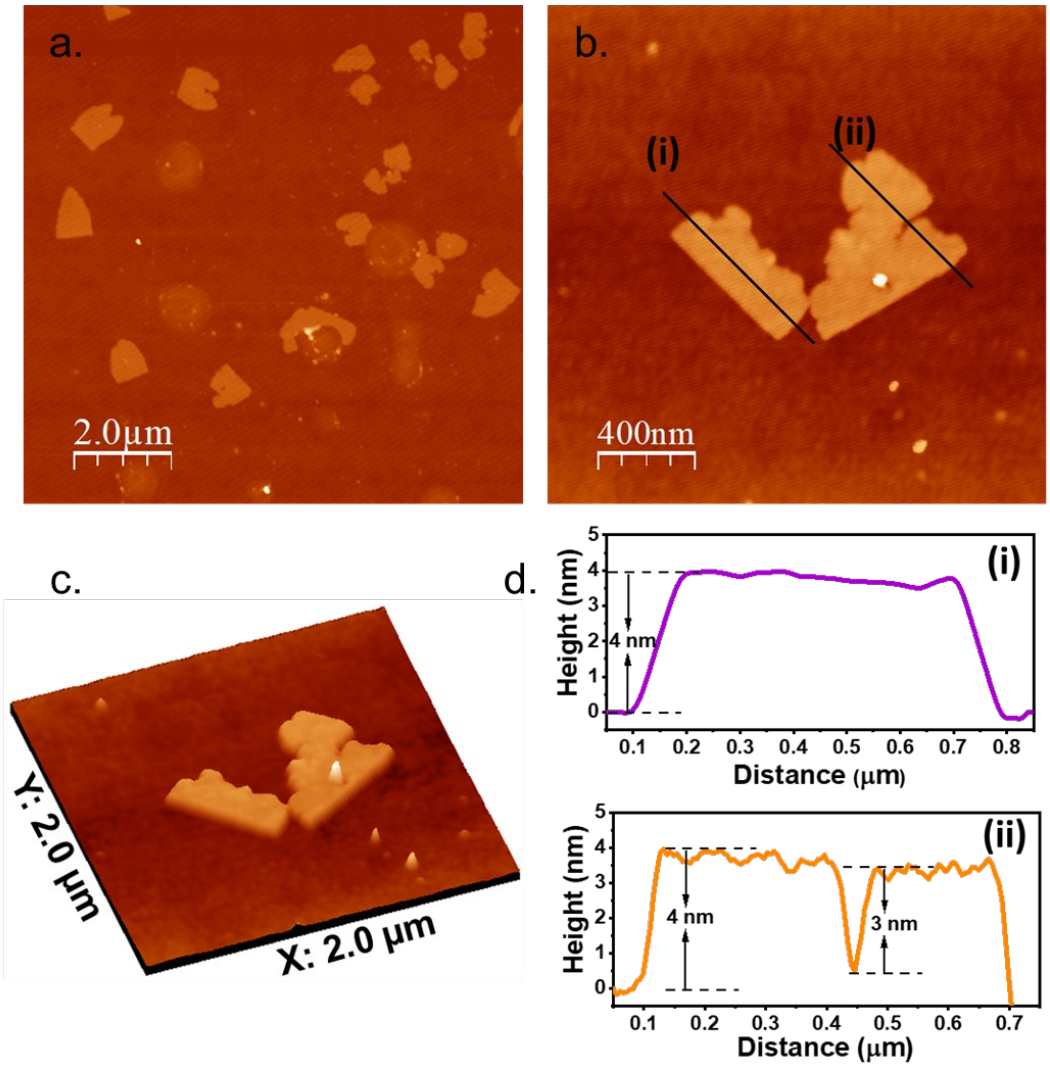

Figure 2. (a,b): AFM scan 2D profiles of the 4h HEBM MgB_2 sample; (c) AFM scan 3D profile, and (d) height profiles revealing the thickness of the nanosheets ranging from 3 - 4 nm, indicating the ultra-thin 2D nature of the exfoliated MgB_2 nanosheets.

The morphology and the crystalline nature of the nanosheets were probed by TEM/HR-TEM and FFT measurements, which confirm that the as-synthesized MgB_2 nanosheets are ultra-thin

and transparent to the high-energy electron beam. Typical TEM images of the exfoliated MgB_2 nanosheets are shown in Figures 3(a) and 3(b) and show lateral dimensions less than 500 nm and mostly flat nanosheets. The nanosheets shown in Figure 3(c) indicate no wrinkles, folds, and crumples.[82,83] These structures appear different from the nanosheets obtained through the liquid-phase exfoliation route shown in our previous study,[59] which had multiple folds and wrinkles. HR-TEM image of the exfoliated MgB_2 nanosheets shown in Figure 3(c) confirms the crystalline nature, and Figure 3(d) reveals the presence of several nanocrystallites, indicating that HEBM has ruptured the bonds in MgB_2 and created more grain boundaries and defects that could potentially serve as active sites for hydrogenation (additional TEM/HR-TEM/EDS images are shown in the SI as Figures S3-S5).[84] The Fast Fourier Transform (FFT) image shown in the inset of Figure 3(d) also indicates that the exfoliated MgB_2 nanosheets are polycrystalline. One can expect that such ultra-thin MgB_2 nanosheets with several grain boundaries and defects would hydrogenate to form $Mg(BH_4)_2$ at a lower pressure and temperature compared to bulk MgB_2, which can only be hydrogenated at high pressure (95 MPa) and high temperature (400 °C).[85]

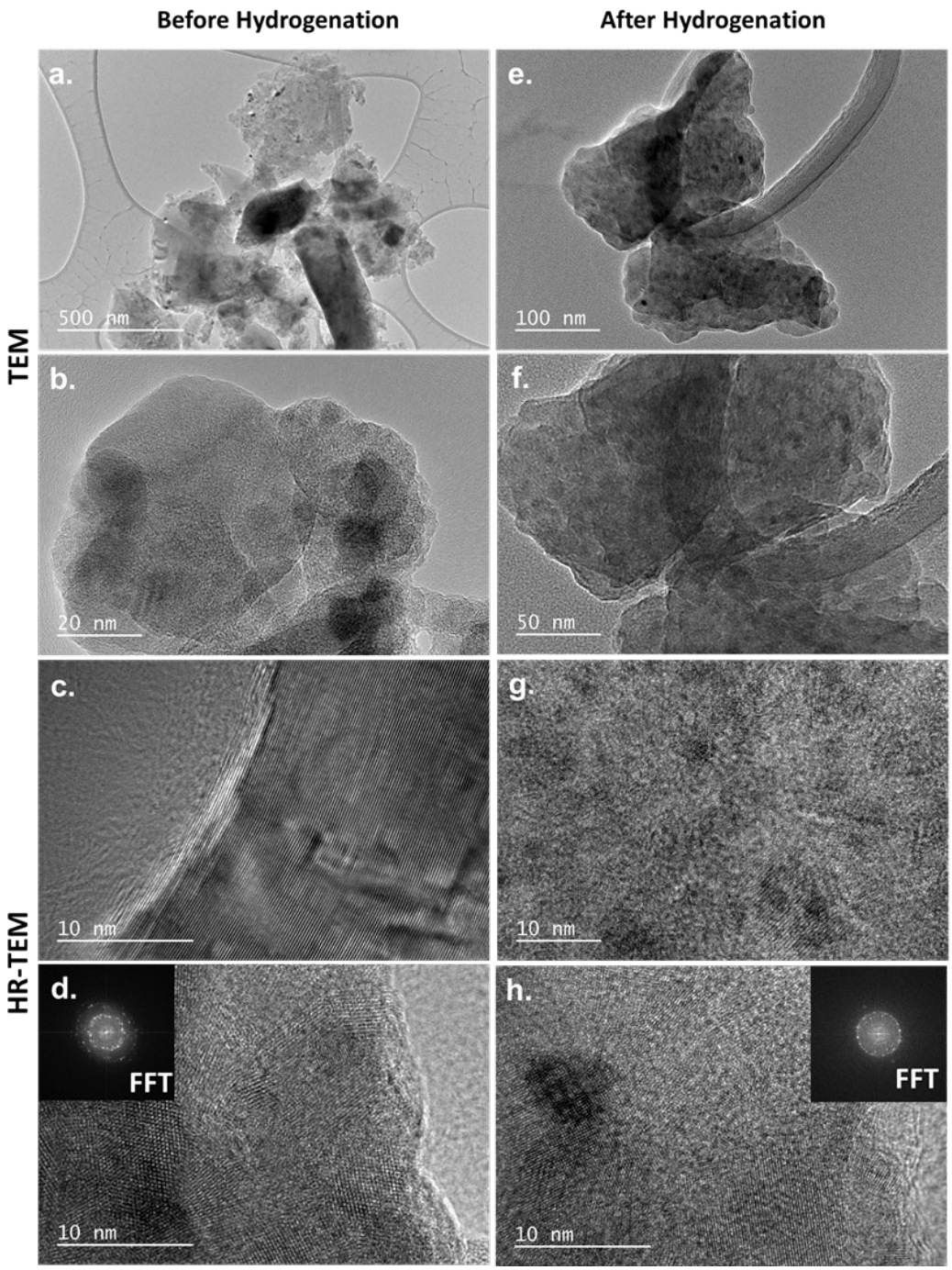

Figure 3. TEM/HR-TEM images with FFT showing the exfoliated MgB_2 nanosheets obtained by milling in zirconia vessel for 4 hours. Micrographs of exfoliated MgB_2 nanosheets (a-d) before high-pressure hydrogenation and (e-h) after high-pressure hydrogenation (70 MPa, 330 °C, 48 hours).

Additional insights into the morphology and elemental composition of the nanosheets were obtained by XPS, FE-SEM, elemental mapping, EDS, and ICP-OES analysis. FE-SEM images shown in SI as Figure S6(a-d) indicate that the particle size of MgB_2 is greatly reduced by HEBM, with nanostructures of less than 500 nm in lateral dimensions, in agreement with the TEM and AFM data. From the XPS analysis of the exfoliated MgB_2 nanosheets shown in Figure 4(a) and 4(b), we found that the Mg 1s (1303.8 eV) and B 1s (186.8 eV) spectra match well with those observed from bulk MgB_2.[81] The B 1s XPS peak at 191.5 eV corresponds to oxidized surface B-OH species, as discussed previously.[58] From the EDS analyses shown in SI as Figure S7, it was found that these nanosheets comprise B and Mg with a B:Mg ratio of 1.72, with small levels of O, Zr, and C. The lower B:Mg ratio in EDS could be due to MgB_2 surface topology effects. The corresponding EDS elemental mapping of the exfoliated MgB_2 nanosheets are presented in the SI as Figure S8. ICP-OES analysis shown in SI as Table S1, reveals that the B:Mg ratio of the nanosheets is actually close to 2:1, which nearly matches the stoichiometry of as-received MgB_2 (B:Mg = 2:00:1.07). These results suggest that the as-synthesized MgB_2 nanosheets have only trace amounts of chemical contamination (from the milling vessel), and are nearly stoichiometric MgB_2.

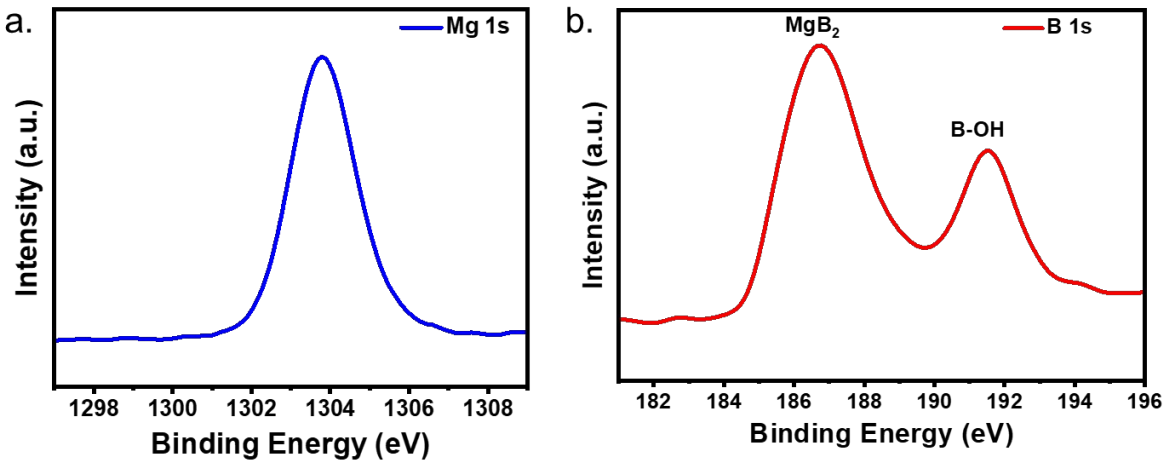

Figure 4. XPS analysis of the exfoliated MgB_2 nanosheets showing the (a) Mg 1s and (b) B 1s spectra indicating the nature of the MgB_2 nanosheets with peaks identified.

To test the hydrogen storage properties of the as-synthesized ultra-thin MgB_2 nanosheets, the samples were hydrogenated under 70 MPa and 330 °C for 48 hours, as well as for an extended time of 168 hours. The pressure and temperature conditions are milder compared to those generally used (90-95 MPa H_2, 390-400 °C) for hydrogenating bulk MgB_2.[85] After removing the samples from the high-pressure hydrogen system (see Figure S9(a)), we observed that the dark-grey powder of MgB_2 nanosheets has partly transformed to a white crystalline phase (see Figure S9(b)). The hydrogenated nanosheets were analyzed using XRD, FTIR, MAS-NMR, XAS, and ICP-OES spectroscopic techniques, as well as high-resolution electron microscopy tools. XRD analysis of the hydrogenated MgB_2 nanosheets (both for 48 h and 168 h samples) are shown in Figure 5(a) compared with bulk MgB_2 and with the exfoliated MgB_2 nanosheets (NS). Hydrogenating these exfoliated MgB_2 nanosheets leads to a new set of diffraction peaks at 2θ values of ~20° characteristic[86] of β-phase $Mg(BH_4)_2$ and a decrease in the intensity of the (101) peak of MgB_2, confirming the conversion of MgB_2 to β-$Mg(BH_4)_2$. Figure 5(b) shows FTIR spectra of the hydrogenated MgB_2 nanosheets compared to bulk MgB_2 and the exfoliated MgB_2 nanosheets prior to hydrogen exposure. We see hydrogenation has produced new absorbance peaks at wavenumbers 1106, 1243, 1370, and 2258 $cm^{-1,}$ indicating the presence of vibrations corresponding to BH_4^- bending and B-H stretching modes.[58,86]

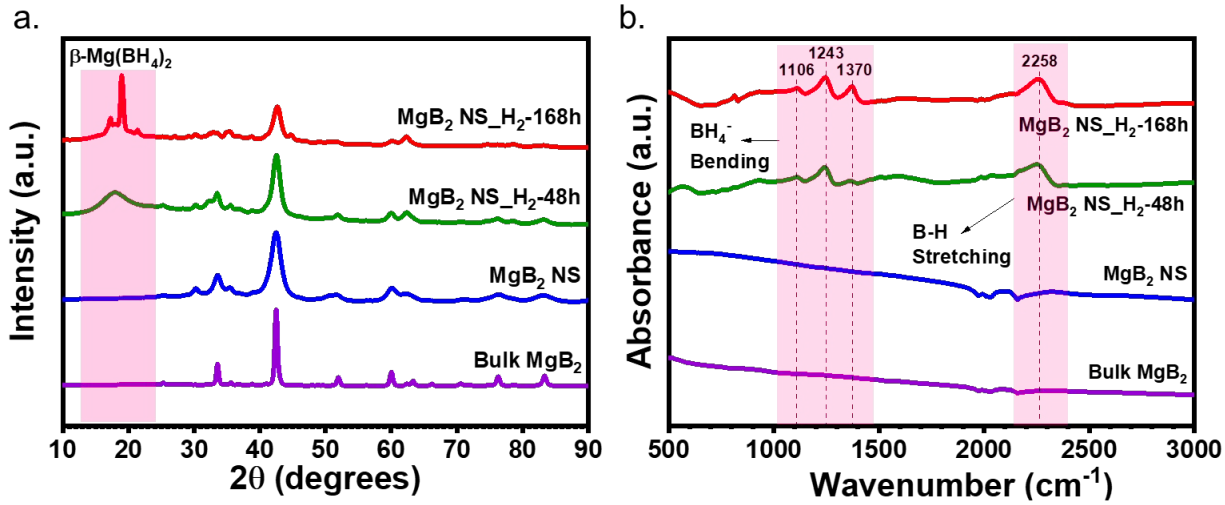

Figure 5. (a) XRD and (b) FTIR analysis of the hydrogenated MgB_2 nanosheets (70 MPa, 330 °C, 48 h, and 700 bar, 330 °C, 168 h) in comparison with bulk MgB_2 and exfoliated MgB_2 nanosheets (t_{BM}:4 h). Both XRD and FTIR measurements confirm the formation of the β-$Mg(BH_4)_2$ phase.

The hydrogenation of MgB_2 nanosheets can potentially form stable intermediate B_xH_y phases like $MgB_{10}H_{10}$ and $MgB_{12}H_{12}$, which are difficult to identify with XRD if they were amorphous. FTIR can identify these phases via absorbance in the ~ 2400 – 2550 cm^{-1} region.[58] Perhaps the most sensitive way to identify such phases is via MAS-NMR analysis. Figure 6(a) compares MAS ^{11}B NMR spectra of hydrogenated MgB_2 nanosheets with bulk MgB_2, MgB_2 nanosheets, and standard β-$Mg(BH_4)_2$. The MAS ^{11}B NMR spectra of bulk MgB_2 and the exfoliated MgB_2 nanosheets show a peak in the range of 90-100 ppm, representing the diboride-like feature that matches well with the data shown in the literature.[47] For the MAS ^{11}B NMR of the hydrogenated MgB_2 nanosheets shown in Figure 6(a), a major peak was found at -41 ppm corresponding to $Mg(BH_4)_2$[47,87] with the peak in the range of 90-100 ppm corresponding to unconverted MgB_2.[47,58] The minor peak at 20 ppm corresponds to a B-O phase,[87] consistent with the XPS data in Figure 4(b). The small peak at -8 ppm was assigned to B_8H_{12},[88] and the peak at -15 ppm corresponds to $[B_{12}H_{12}]^{2-}$ species.[89] Summarizing, MAS ^{11}B NMR analysis has confirmed that the exfoliated MgB_2 nanosheets hydrogenate to borohydride at a significantly lower pressure (70 MPa) and temperature (330 °C) than generally required for bulk MgB_2 hydrogenation (90-95 MPa and 390-400 °C). The ICP-OES results of the hydrogenated nanosheets shown in the SI as Table S1 indicate that the Mg:B ratio remained as ~1:2 after hydrogenation, which implies that no significant amounts of volatile B_xH_y boranes form under these conditions.

TEM/HR-TEM and FE-SEM analysis was used to probe how the morphology of the MgB_2 nanosheets changes after hydrogenation. From the TEM/HR-TEM images shown in Figure 3(e-h), we found the presence of small dot like structures on the nanosheets indicating the formation of borohydride crystalline phases on the MgB_2 nanosheets. More such TEM/HR-TEM images are shown in SI as Figure S10. From the FE-SEM microscopic images shown in SI as Figure S6(e-h), we observed a drastic change in the morphology of the nanosheets upon hydrogenation, the nanosheets were found to be flaky, rugged, agglomerated, and porous in nature.

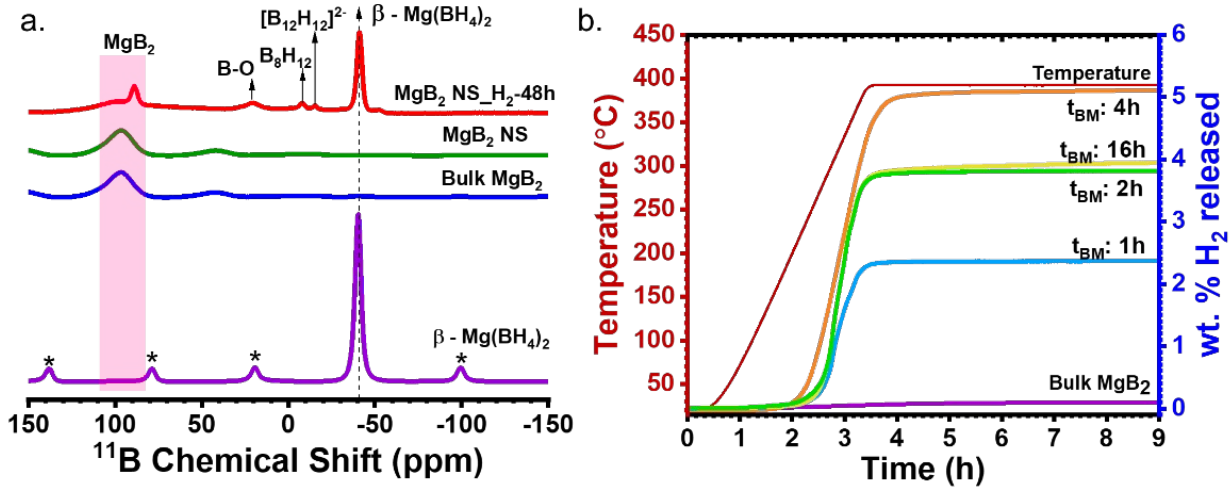

Figure 6. (a) MAS ^{11}B NMR analysis. The MAS ^{11}B NMR spectra of the 48h hydrogenated MgB_2 nanosheets in comparison with MgB_2 NS, bulk MgB_2, and standard β-$Mg(BH_4)_2$ showing the formation of β-$Mg(BH_4)_2$ as the major phase and B-O, B_8H_{12}, and $[B_{12}H_{12}]^{2-}$ as minor phases along with the presence of some unreacted MgB_2 phase. (b) Sieverts dehydrogenation studies of the hydrogenated MgB_2 nanosheets (hydrogenated at 70 MPa, 330 °C, 48 h) obtained at various hours of milling (t_{BM}: 1, 2, 4, and 16 h) compared with bulk MgB_2 showing the wt. % of H_2 released as a function of temperature (up to 390 °C) and time (up to 9 hours).

To probe the kinetics of hydrogen release, we performed Sieverts dehydrogenation studies by heating the hydrogenated samples to 390 °C and monitoring the change in pressure as a function of temperature. Figure 6(b) reports dehydrogenation results for samples with varying t_{BM}. The mass of hydrogen released from the hydrogenated samples of bulk MgB_2, as well as 1, 2, 4, and 16 h milled samples was found to be 0.1, 2.4, 3.8, 5.1, and 3.9 wt. % hydrogen, respectively. Surprisingly, the MgB_2 nanosheets obtained after 4 h of milling have shown the highest reversible hydrogen capacity of 5.1 wt.% H_2 upon dehydrogenation at 390 °C, whereas the amount of hydrogen released for the 16 h milled sample was diminished to ~0.8 times the value of the 4 h milled sample, which could be due to the sintering effect that happens with over milling, as suggested by the XRD results shown in Figure 1. Under similar conditions, the product of bulk MgB_2 hydrogenation released only 0.1 wt. % hydrogen. Thus, exfoliating bulk

MgB_2 into ultra-thin MgB_2 nanosheets has increased the hydrogen storage capacity of MgB_2 by ~50 times.

The ~50x improvement in hydrogen storage capacity can be rationalized with consideration of the MgB_2 nanosheet dimensions. A typical NS, roughly 500 x 500 x 4 nm from the AFM measurements (Figure 2), is approximately 11 - 12 MgB_2 layers thick. The 5.1 wt. % hydrogenation capacity corresponds to the hydrogenation of 4 layers, or 2 layers on each side. Bulk MgB_2 samples can be ~ 500 x 500 x 200 nm in size,[79] so the increased hydrogen capacity of the MgB_2 nanosheets can be explained by the increased surface to volume ratio. In other words, splitting a 200 nm thick bulk MgB_2 stack into fifty 4 nm-thick sheets roughly multiplies the surface area by 50 and so the hydrogen uptake would then scale with surface area, instead of volume. This indicates a hydrogenation depth to 2 layers for each exposed surface, bulk or nanomaterial, and suggests a self-limited process consistent with earlier studies[43] on initial stages of MgB_2 hydrogenation.

The lowest energy surface of MgB_2 is the (001) Mg-terminated basal plane.[90] However, the MgB_2 nanosheets cannot all be Mg-terminated because that would violate the stoichiometry of the parent material. Thus, the nanomaterial surfaces must have closer to the stoichiometry of the bulk material because the nanomaterial has a significant proportion of surface atoms. Indeed, a near bulk 1:2 Mg:B stoichiometry of the MgB_2 nanosheets was observed in SI as Figure S7 (FE-SEM/EDS data) and Table S1 (ICP-OES data). In contrast, a B-deficient Mg-B nanosheets material ($MgB_{0.75}$) was produced via surfactant ball milling of bulk MgB_2.[58]

Lower concentrations of Mg on the surface are known to destabilize the surface B layer. In the case of an entirely B-terminated MgB_2 (001) surface, Li et al. have predicted[91] with DFT calculations that the surface boron layer will spontaneously disorder to lower its energy. This disordering occurs due to a weakening in the surface B-B hexagonal bond network and could enable greater hydrogen absorption. Building on that analysis to get an idea of the disordering tendencies of the upper boron layer in the presence of non-zero amounts of surface Mg, we performed calculations with varying Mg surface coverage to determine the stability of that surface compared to a disordered B-terminated surface, which is 32 meV A^{-2} lower in energy

than the pristine B-terminated basal surface. [91] We calculated energies for the 0.25, 0.33, 0.66, and 0.75 Mg coverages, with a coverage of 1.0 corresponding to Mg-terminated and zero coverage corresponding to B-terminated. Symmetrically distributed Mg coverages were found to be lower energy than segregating the surface into portions entirely B-terminated and entirely Mg-terminated, except for the 0.66 case where the surface formation enthalpies for these cases (clumping Mg vs. evenly distributed) were nearly isoenergetic (within 1 meV A^{-2}). However, if we consider instead surfaces that segregate into Mg-terminated portions and disordered B-terminated surfaces, for all cases the segregated structure is lower energy, indicating a thermodynamic drive toward both segregation of surface terminations and boron disordering. These surface energy comparisons are shown in Figure 7(a).

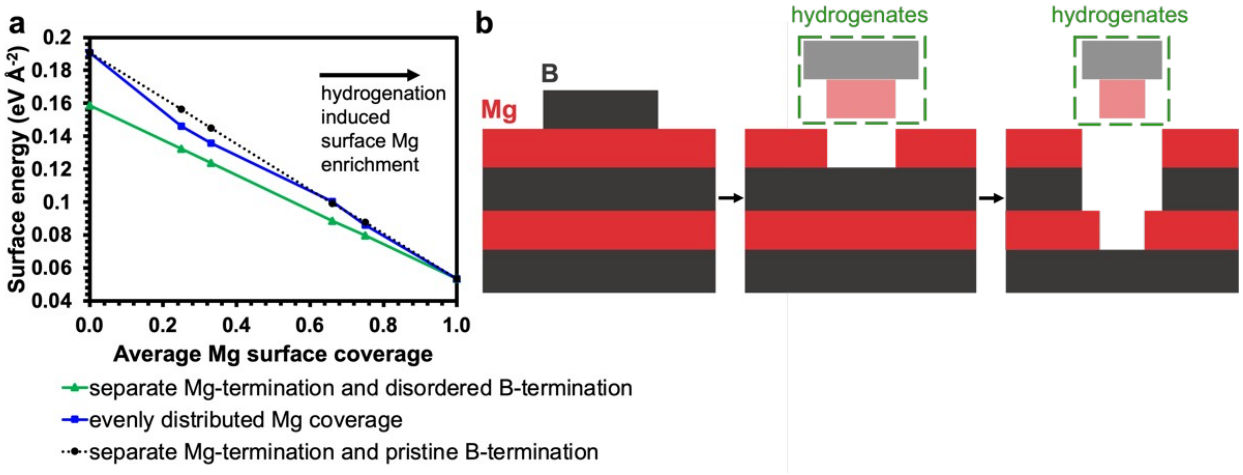

Figure 7. (a) Comparisons of MgB_2 surface energy depending on the spatial distribution of surface Mg, surface B structure, and Mg surface coverage ratio. (b) Proposed process of self-limited hydrogenation wherein a thermodynamic drive causes Mg to be left behind on the MgB_2 surface as the material hydrogenates. Greater surface Mg coverage is expected to slow MgB_2 hydrogenation kinetics by increasing the stability of the outer-most B hexagonal sheet. In our schematic, the MgB_2 surface starts with ½ Mg termination and ½ B termination and ends with an almost fully Mg-terminated terraced surface as the MgB_2 material is eroded during hydrogenation.

We conclude that any amount of Mg will stabilize a part of the surface of proportional area. Similar behavior has been observed in DFT molecular dynamics simulations of hydrogenation

that revealed that the boron ring stability on the $(10\acute{1}0)$ edge of MgB_2 increased with the presence of surface Mg and Mg inhibited hydrogenation compared to a surface with less Mg.[92] Furthermore, that study showed that the balance of Mg on the surface may change as the material hydrogenates because it is energetically favorable to trade a slightly lower than 1 Mg : 2 B product phase for greater Mg coverage on the MgB_2 surface. This is possible because depending on the surface to volume ratio, a small percentage change in the hydrogenated product Mg : B ratio can create a larger change in stoichiometry of the MgB_2 terminal surface layer, keeping the overall stoichiometry (reactant and product) constant. This process would also be consistent with the presence of a small amount of material in the product with a lower Mg : B ratio, such as the $MgB_{12}H_{12}$ material detected with NMR (Figure 6(a)) after hydrogenation, alongside stoichiometric $Mg(BH_4)_2$ in the product phase. Our proposed process to explain decreasing hydrogenation rate is schematically depicted in Figure 7(b): as MgB_2 is eroded during hydrogenation, a small amount of Mg is left behind at each step, increasing surface stability and slowing the kinetics of further hydrogenation.

The powder consisting of the dehydrogenated material from the Sievert's apparatus (shown in SI as Figure S9(b)) was collected and further studied under XRD, FTIR, and FE-SEM to understand the chemical and physical transformations that occur with hydrogen adsorption/desorption cycling. The XRD studies shown in Figure 8(a) indicate that after dehydrogenation, the $Mg(BH_4)_2$ phase completely disappeared and directly transformed into crystalline Mg,[48] amorphous boron, and MgB_2 phases. From the FTIR analysis shown in the SI as Figure S11, we further confirmed that the vibrations of B-H stretching and BH_4^- bending corresponding to a $Mg(BH_4)_2$ phase disappeared upon dehydrogenation, and no further significant vibrations were observed, indicating the elimination of $Mg(BH_4)_2$ upon hydrogen release. The FTIR spectra of bulk MgB_2, exfoliated MgB_2 nanosheets before and after hydrogenation, along with standard $Mg(BH_4)_2$ and $MgB_{12}H_{12,}$ are also presented for a comparison in the SI as Figure S11. The dehydrogenated MgB_2 nanosheets transform from flaky, rugged, and porous to smooth nanostructures, similar to the morphology of MgB_2 nanosheets before hydrogenation.

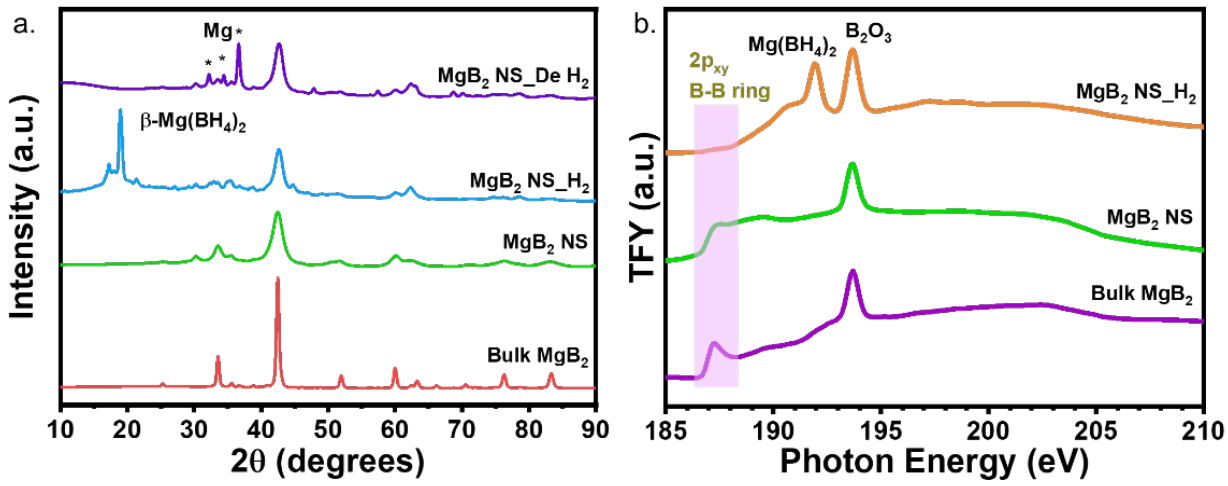

Figure 8. (a) XRD analysis of the dehydrogenated MgB_2 nanosheets compared to bulk MgB_2 and MgB_2 nanosheets before and after hydrogenation. With dehydrogenation, the β-$Mg(BH_4)_2$ phase is converted into crystalline Mg and MgB_2 phases. (b) B K-edge XAS spectra of the hydrogenated MgB_2 nanosheets compared to bulk MgB_2 and as-prepared MgB_2 NS. The B $2p_{xy}$ B-B ring feature at ~187 eV and the formation of $Mg(BH_4)_2$ phase at ~192 eV upon hydrogenation is highlighted.

X-ray absorption spectroscopy (XAS) measurements on the MgB_2 nanosheets before and after hydrogenation provide additional mechanistic insights into the hydrogenation process. From the boron K-edge spectra recorded in TFY mode shown in Figure 8(b), there is a distinct feature at a photon energy of ~187 eV corresponding to the $2p_{xy}$ B-B ring feature of MgB_2.[43] We found that the peak is broadened in the case of exfoliated MgB_2 nanosheets compared to bulk MgB_2 indicating the distortion of the stable B-B ring structure. This distortion can be rationalized by formation of new grain boundaries, lattice defects, and dangling bonds upon milling, which then create more active sites for MgB_2 hydrogenation.[43] The peak at ~187 eV completely disappeared upon hydrogenation, indicating significant disruption of the boride B-B hexagonal ring structure. The new peak at ~192 eV indicates the formation of the $Mg(BH_4)_2$ phase upon hydrogenation, consistent with the MAS NMR, FTIR, and XRD results.

3. Conclusions

This study reports a solvent-free mechanochemical exfoliation of strongly-bonded MgB_2 layers using high-energy ball milling (HEBM), which results in MgB_2 nanosheets of ~3 - 4 nm in thickness. The developed synthesis method is simple, easily scalable, and yields MgB_2 nanosheets with low degree of contamination. Exfoliating MgB_2 into 2D nanosheets using HEBM produces nanoscale MgB_2 with a high density of grain boundaries, lattice defects, and dangling bonds by disrupting the stable B-B ring structure. These modifications ease the pressure and temperature requirements to hydrogenate MgB_2. The MgB_2 nanosheets produced after 4 hours of HEBM can be hydrogenated at a relatively low H_2 pressure (70 MPa) and temperature (330 °C) within 48 hours, whereas bulk MgB_2 hydrogenates at 95 MPa, 400 °C, and 108 hours.[43,58] We found that the hydrogenated MgB_2 nanosheets release a remarkable amount of hydrogen (~5.1 wt. %) upon thermal treatment, which is ~50 times higher than in the case of bulk MgB_2.

The MgB_2 nanosheets reported here are physically different than the exfoliated material produced by surfactant-assisted ball milling reported previously by Liu and co-workers.[58] In the present study, the magnesium boride nanosheet material is nearly stoichiometric (Mg:B = 1:2), has laterally large sheet domains (~ 500 nm), has no surfactant on the surface, and displays an observable (though broadened) B $2p_{xy}$ feature in the XAS. In contrast, the Mg-B material produced by surfactant ball milling is B-deficient ($MgB_{0.75}$), has lateral sizes ranging from 5 to 50 nm, and shows no sign of a B $2p_{xy}$ feature in the XAS. Both materials showed an improvement in hydrogenation compared to bulk MgB_2, which highlights the importance of understanding nanoscale effects in 2D materials.

One can envision that single- or few-atomic layers of MgB_2 could be isolated and hydrogenated under even milder conditions of hydrogen pressure and/or temperature. Moreover, the synthesis strategy presented here to exfoliate MgB_2 using HEBM could be extended to other strongly bonded layered metal borides.[93,94] The ultra-thin MgB_2 nanosheets in nearly pristine

form could have applications beyond solid-state hydrogen storage, for example in superconductivity, sensing, electronics, batteries, and electrocatalysis.[95] The scalable synthesis of phase-pure metal boride nanosheets using economical solid-state exfoliation routes could be an important step in enabling their full potential to solve challenging materials science problems.

4. Experimental and Theoretical Methods

Synthesis and preparation of MgB_2 nanosheets: Sample preparation and handling were conducted at the Sandia National Laboratories site in California (SNL-CA) in an Ar-filled glovebox equipped with a recirculation system that keeps H_2O and O_2 concentrations below 0.1 ppm. As-received MgB_2 powder (Sigma-Aldrich, ≥ 99% purity) was subjected to solid-state mechanical exfoliation using a high-energy ball mill (HEBM, SPEX SamplePrep, 8000M Mixer/ Mill). The milling was carried out in a zirconia (ZrO_2) vial using 8 mm diameter ZrO_2 balls. Briefly, 0.800 g of as-received MgB_2 powder and ~20.16 g of ZrO_2 balls were weighed in the argon glovebox and added to the milling vial to obtain a ball-to-powder weight ratio of ~25:1. The milling vial was closed tightly in the argon glovebox and then subjected to HEBM for ball-milling times (t_{BM}) of 1, 2, 4, and 16 hours. The milled powders were collected and stored in an argon glovebox.

XRD: The powder X-ray diffraction (XRD) measurements were made on an Oxford Diffraction Supernova in capillary mode using Cu K_α radiation, with a CCD detector at 77 mm from the samples with an exposure time of 66 seconds. The recorded 2D diffraction images were integrated to produce a 1D diffraction spectrum. The powder samples were packed in 0.5 mm glass capillaries sealed with silicone grease under the argon environment. The crystallize size was determined using the Debye-Scherrer formula: $D = \frac{0.9\lambda}{\beta \cos\theta}$

where D = average crystallite size, λ-wavelength of X-ray Cu K_α = 1.542 Å, β = full-width half maxima in radians, and θ = Bragg angle in degrees. [67]

TEM, HRTEM, and EDS: Transmission electron microscopy (TEM), high-resolution TEM (HRTEM) imaging and energy-dispersive X-ray spectroscopy (EDS) were recorded on a Thermo Fisher Titan Themis Z TEM operated at 300 kV. The MgB_2 nanosheets (t_{BM}:4h) powder sample was dispersed in ~10 mL of anhydrous IPA and then bath sonicated for 5 minutes before drop-casted on a lacey carbon film supported on a 300-mesh copper TEM grid (Ted Pella, Inc.). The grid with the sample was air-dried for a few minutes and stored in a vial until analysis. Additional TEM/HRTEM images were obtained at the Molecular Foundry at Lawrence Berkeley National Laboratory (LBNL), using a Jeol 2100-F 200 kV field-emission microscope. The HEBM MgB_2 nanosheets (t_{BM} = 4 hours) powder sample was dispersed in Tetrahydrofuran (THF) inside the glovebox and then sonicated for 5 minutes before being drop-casted on a lacey carbon film supported TEM grid. The grid with the sample was air-dried for a ~ 1 minute before putting it onto the sample holder for imaging.

XAS: Soft X-ray absorption (XAS) spectra were collected on beamlines 7.3.1 and 8.0.1 at Advanced Light Source (ALS). B K-edge XAS spectra were recorded in total electron yield (TEY) and total fluorescence yield (TFY) modes simultaneously with 0.2 eV FWHM energy resolution under ultra-high vacuum (UHV) at ~ 1 $x10^{-9}$ Torr. XAS spectra were energy calibrated to the B–O π^* resonance (194.0 eV) of a B_2O_3 standard powder before and after the experiment, with the data analyzed as described previously.[43] The samples were mounted in an argon glovebox and transferred to the experimental XAS chamber without exposing to the atmosphere.

MAS-NMR: Magic Angle Spinning (MAS)-Nuclear Magnetic Resonance (NMR) studies were conducted at Lawrence Livermore National Laboratory (LLNL). The Larmor frequency was 192.54 for ^{11}B. The samples were packed in an argon glovebox within a 2.5 mm ZrO_2 rotor and spun at 25 kHz. A hard pulse ($\pi/12$) length of 0.5 μs was used for ^{11}B (B1 field strength 500 kHz). A Recycle delay of 0.5 s was used. ^{11}B chemical shifts were externally referenced to boric acid (δ_{iso} =19.6 ppm).

AFM: Atomic Force Microscope (AFM) images were acquired with a Dimension ICON (Bruker) contained in an argon glovebox. The AFM was operated in Peak-Force Tapping mode

with a nominal tapping force of 1 nN. The tip used was a PFQNE-AL (Bruker) with a spring constant of 0.84 nN/nm. Sample for AFM analysis was prepared by static dispensing of the MgB_2 NSs/IPA dispersion (~20 µL) on a cleaned and UV Ozone treated Si/SiO_2 substrate and spin-coated at a speed of 3000 rpm for 30 s at a ramp rate of 100. The coated substrate was stored in an argon environment until AFM analysis.

FTIR: Fourier transform infrared (FTIR) spectra were obtained using an Agilent Cary-630 spectrometer, with an attenuated total reflectance (ATR) module containing a diamond crystal. The FTIR was located inside an argon glovebox to prevent exposure to air and moisture.

FE-SEM and EDS: The morphology and elemental composition of the MgB_2 NSs samples were analyzed with a field-emission scanning electron microscope (FE-SEM from JEOL JSM-7600F, USA) operated at 5-15 kV, located at SNL and IIT Gandhinagar (IITGN). All the samples were sputter-coated with platinum at 10 mA for 90 seconds under vacuum prior to analysis.

High-pressure hydrogenation: Experiments were performed at SNL-CA in a custom high-pressure reactor with a Newport Scientific compressor and a vessel made from 316L stainless-steel components. Samples were loaded inside an argon glovebox (< 0.1 ppm H_2O, < 0.1 ppm O_2). Cylindrical stainless-steel slugs were placed at the bottom of the vessel so that up to four crucibles could be loaded into the vessel simultaneously, with all crucibles remaining in the main heating zone. The system was initially pressurized with hydrogen (Matheson Tri-Gas, 99.9999% purity) to reach the target pressure of 70 MPa. The samples were heated using a furnace surrounding the vessel to 330 °C, with the reported temperatures measured at the outside surface of the vessel with a type K thermocouple. The conditions were held isothermal and isobaric for 48 h, 168 h, and then the system was cooled to ambient temperature before releasing the pressure to avoid hydrogen desorption.

Sievert's measurements: Hydrogen storage capacity measurements were conducted on Setaram's PCT-Pro instrument at SNL-CA. The hydrogenated MgB_2 nanosheet powder samples were weighed and loaded into an air-tight stainless-steel sample holder under an argon atmosphere. The sample holder was connected to the Sievert's system and evacuated before heating was begun. Moreover, the volume calibration was performed before the measurement.

The sample was heated using a furnace enclosing the sample holder and desorption took place into a vacuum chamber of known volume. The sample was heated to a maximum temperature of 390 °C. In interpreting the mass loss data upon desorption, H_2 was assumed to be the only gaseous product of the reaction.

ICP-OES: Inductively coupled plasma-optical emission spectroscopy (ICP-OES) was used to measure the concentration of Mg and B in the exfoliated, hydrogenated, and dehydrogenated MgB_2 nanosheets. The analysis was performed using a PerkinElmer Avio 200 instrument located at IIT Gandhinagar. Before the analysis, the samples were digested overnight in a 2% HNO_3 solution. Briefly, ~4 mg of the sample was measured and added to 100 mL of 2% HNO_3 and allowed to digest overnight. All the samples were found to be digested completely without any sediments. The samples were further diluted 40 times using 2% HNO_3 just before the analysis.

XPS: XPS measurements were conducted at LBNL's Molecular Foundry. The K-Alpha Plus instrument utilized a monochromatic Al K_α X-ray source with a 400 μm spot size and a low-energy electron flood source for charge neutralization. Powder samples were pressed into silver tape or silicon within an argon glovebox and loaded into the instrument using an air-free vacuum transfer holder. For all samples, the C 1s XPS peak of adventitious C contamination was used as an internal binding energy reference standard at 284.48 eV.

DFT Studies: Density functional theory (DFT) calculations were performed using the Vienna Ab initio Simulation Package (VASP)[68-70] with a plane-wave cutoff of 400 eV and forces were relaxed to below 0.005 eV/Å. MgB_2 (001) surface formation energies were calculated for different surface coverages of Mg, 0, 0.25, 0.33, 0.66, 0.75, and 1.0, using slab geometries with in-plane dimensions of (3 X 3) surface units (for 0.33, 0.66 Mg-coverage with 4x4x1 k-point sampling) or (4 X 4) surface units (for 0, 0.25, 0.75, 1.0 Mg-coverage with 3x3x1 k-point sampling) and a thickness of 9 layers with 16.7 Å of vacuum between slabs. Projector augmented wave (PAW) pseudopotentials[71] and the Perdew-Burke-Ernzerhof (PBE) density functional[72] were employed. Surface energies were referenced to bulk MgB_2 and Mg-metal.

Conflict of Interest

The authors declare no competing financial interest.

Data Availability Statement

The data that support the findings of this study are available upon request.

Keywords

Nanosheets, metal borides, exfoliation, hydrogen storage, metal borohydrides.

Acknowledgments

The authors acknowledge financial support through the Hydrogen Storage Materials Advanced Research Consortium (HyMARC) of the U.S. Department of Energy (DOE), Office of Energy Efficiency and Renewable Energy, Fuel Cell Technologies Office under Contracts DE-AC52-07NA27344 and DE-AC04-94AL85000. Part of the work was performed under the auspices of the DOE by Lawrence Livermore National Laboratory under Contract DE-AC52-07NA27344. Sandia National Laboratories is a multi-mission laboratory managed by National Technology and Engineering Solutions of Sandia, LLC, a wholly owned subsidiary of Honeywell International Inc., for the DOE's National Nuclear Security Administration under contract DE-NA0003525. Portions of this research were performed on BLs 7.3.1 and 8.0.1 at the Advanced Light Source, Lawrence Berkeley National Laboratory, which is supported by the Director, Office of Science, Office of Basic Energy Sciences, of the U.S. DOE under Contract DE-AC02–05CH11231. XPS work at the Molecular Foundry of the Lawrence Berkeley National Laboratory was supported by the Office of Science, Office of Basic Energy Sciences, of the U.S. Department of Energy under Contract No. DE-AC02-05CH11231. H.G. gratefully acknowledges the support from IIT Gandhinagar Overseas Research Experience Fellowship. The authors also acknowledge the funding support from Core Research Grant (No. EMR/2017/000730) by the Department of Science and Technology India; INSPIRE Faculty Award Research Grant (No.

DST/INSPIRE/04/2014/001601), Department of Science and Technology, India; Seed Funding from IIT Gandhinagar; and Dr. Dinesh O. Shah chair funding.

The views and opinions of the authors expressed herein do not necessarily state or reflect those of the United States Government or any agency thereof. Neither the United States Government nor any agency thereof, nor any of their employees, makes any warranty, expressed or implied, or assumes any legal liability or responsibility for the accuracy, completeness, or usefulness of any information, apparatus, product, or process disclosed, or represents that its use would not infringe privately owned rights.

References:

(1) Global Energy Review 2021 – Analysis - IEA; https://www.iea.org/reports/global-energy-review-2021 (accessed June 27, 2022).

(2) L.E. Klebanoff, J.O. Keller, M.H. Fronk and P. Scott, *"Hydrogen Conversion Technologies and Automotive Applications,"* Chapter 2 in "*Hydrogen Storage Technology, Materials and Applications*", Ed. L.E. Klebanoff, (Taylor and Francis, Boca Raton, 2012) p. 31.

(3) Rath, R.; Kumar, P.; Mohanty, S.; Nayak, S. K. Recent advances, unsolved deficiencies, and future perspectives of hydrogen fuel cells in transportation and portable sectors. *Int. J. Energy Res*. **2019**, *43*, 8931–8955.

(4) Madsen, R.T., Klebanoff, L.E., Caughlan, S.A.M., Pratt, J.W., Leach, T.S., Appelgate Jr. "Feasibility of the Zero-V: A Zero-emissions Hydrogen Fuel-cell Coastal Research Vessel," *Int. J. Hydrogen Energy,* **2020**, *45*, 25328–25343

(5) Ley, M.B., Jepsen, L.H., Lee, Y.-S., Cho, Y.W., Bellosta von Colbe, J.M., Dornheim, M. Complex Hydrides for Hydrogen Storage- New Perspectives, *Mater. Today*, **2014**, *17*, 122–128.

(6) Eberle, U.; Felderhoff, M.; Schüth, F. Chemical and Physical Solutions for Hydrogen

Storage. *Angew. Chem. Int. Ed.* **2009**, *48*, 6608–6630.

(7) Chao, B. and Klebanoff, L.E., "Hydrogen Storage in Interstitial Metal Hydrides," in "*Hydrogen Storage Technology, Materials and Applications*", (Taylor and Francis, Boca Raton 2012), p. 109.

(8) Li, H. W.; Yan, Y.; Orimo, S. I.; Züttel, A.; Jensen, C. M. Recent Progress in Metal Borohydrides for Hydrogen Storage. *Energies* **2011**, *4*, 185–214.

(9) Suresh, K., Aulakh, D., Purewal, J., Siegel, D.J., Veenstra, M.; Matzger, A.J., Optimizing Hydrogen Storage in MOFs through Engineering of Crystal Morphology and Control of Crystal Size*, J. Am. Chem. Soc.* **2021**, *143*, 10727–10734.

(10) Wood, B.C., Stavila, V., Poonyayant, N., Heo, T.W., Ray, K.G., Klebanoff, L.E., et al. Nanointerface-driven Reversible Hydrogen Storage in the Nanoconfined Li-N-H System*, Adv. Mat. Interfaces*, **2017**, *4*, 1600803.

(11) The DOE hydrogen storage system technical targets for light-duty fuel cell vehicles were established by the DOE in consultation with the Freedom CAR and Fuel Partnership Program. They can be found at: https://www.energy.gov/eere/fuelcells/doe-technical-targets-onboard-hydrogen-storage-light-duty-vehicles

(12) Schneemann, A.; White, J. L.; Kang, S.; Jeong, S.; Wan, L. F.; Cho, E. S.; Heo, T. W.; Prendergast, D.; Urban, J. J.; Wood, B. C.; Allendorf, M. D.; Stavila, V. Nanostructured Metal Hydrides for Hydrogen Storage. *Chem. Rev.*, **2018**, *118*, 10775–10839.

(13) Yu, X.; Tang, Z.; Sun, D.; Ouyang, L.; Zhu, M. Recent Advances and Remaining Challenges of Nanostructured Materials for Hydrogen Storage Applications. *Prog. Mater. Sci.*, **2017**, *88*, 1–48.

(14) Stavila, V.; Li, S.; Dun, C.; Marple, M. A. T.; Mason, H. E.; Snider, J. L.; Reynolds, J. E.; El Gabaly, F.; Sugar, J. D.; Spataru, C. D.; Zhou, X. W.; Dizdar, B.; Majzoub, E. H.; Chatterjee, R.; Yano, J.; Schlomberg, H.; Lotsch, B. V.; Urban, J. J.; Wood, B. C.; Allendorf, M. D. Defying Thermodynamics: Stabilization of Alane Within Covalent Triazine Frameworks for Reversible Hydrogen Storage. *Angew. Chem. Int. Ed*. **2021**, *60*, 25815-25824.

(15) Cho, Y.; Li, S.; Snider, J. L.; Marple, M. A. T.; Strange, N. A.; Sugar, J. D.; El Gabaly,

F.; Schneemann, A.; Kang, S.; Kang, M.; Park, H.; Park, J.; Wan, L. F.; Mason, H. E.; Allendorf, M. D.; Wood, B. C.; Cho, E. S.; Stavila, V. Reversing the Irreversible: Thermodynamic Stabilization of Lithium Aluminum Hydride Nanoconfined Within a Nitrogen-Doped Carbon Host, *ACS Nano*, **2021**, *15*, 10163-10174.

(16) Schneemann, A.; Wan, L. F.; Lipton, A. S.; Liu, Y. S.; Snider, J. L.; Baker, A. A.; Sugar, J. D.; Spataru, C. D.; Guo, J. H.; Autrey, T. S.; Jorgensen, J.; Jensen, T. R.; Wood, B. C.; Allendorf, M. D.; Stavila, V. Nanoconfinement of Molecular Magnesium Borohydride Captured in a Bipyridine-Functionalized Metal-Organic Framework, *ACS Nano*, **2020**, *14*, 10294-10302.

(17) Lai, Q.; Wang, T.; Sun, Y.; Aguey-Zinsou, K.-F. Rational Design of Nanosized Light Elements for Hydrogen Storage: Classes, Synthesis, Characterization, and Properties. *Adv. Mater. Technol*. **2018**, *3*, 1700298.

(18) Fichtner, M. Nanotechnological Aspects in Materials for Hydrogen Storage. *Adv. Eng, Mater*. **2005**, *7*, 443–455.

(19) De Jongh, P. E.; Adelhelm, P. Nanosizing and Nanoconfinement: New Strategies towards Meeting Hydrogen Storage Goals. *ChemSusChem*. **2010**, *3*, 1332–1348.

(20) Allendorf, M.D.; Hulvey, Z.; Gennett, T.; Ahmed, A.; Autrey, T.; Camp, J.; Cho, E. S.; Furukawa, H.; Haranczyk, M.; Head-Gordon, M.; Jeong, S.; Karkamkar, A.; Liu, D.-J.; Long, J. R.; Meihaus, K. R.; Nayyar, I. H.; Nazarov, R.; Siegel, D. J.; Stavila, V.; Urban, J. J; Veccham S. P.; Wood, B.C., An assessment of strategies for the development of solid-state adsorbents for vehicular hydrogen storage, *Energy Environ. Sci.,* **2018,** *11*, 2784-2812.

(21) Chen, L.; Cooper, A. C.; Pez, G. P.; Cheng, H. Mechanistic Study on Hydrogen Spillover onto Graphitic Carbon Materials. *J. Phys. Chem. C* **2007**, *111*, 18995–19000.

(22) Du, A.; Zhu, Z.; Smith, S. C. Multifunctional Porous Graphene for Nanoelectronics and Hydrogen Storage: New Properties Revealed by First Principle Calculations. *J. Am. Chem. Soc.* **2010**, *132*, 2876–2877.

(23) Lee, H.; Ihm, J.; Cohen, M. L.; Louie, S. G. Calcium-Decorated Graphene-Based Nanostructures for Hydrogen Storage. *Nano Lett.* **2010**, *10*, 793–798.

(24) Antipina, L. Y.; Avramov, P. V.; Sakai, S.; Naramoto, H.; Ohtomo, M.; Entani, S.; Matsumoto, Y.; Sorokin, P. B. High Hydrogen-Adsorption-Rate Material Based on Graphane Decorated with Alkali Metals. *Phys. Rev. B - Condens. Matter Mater. Phys.* **2012**, *86*, 085435.

(25) Seayad, A. M.; Antonell, D. M. Recent Advances in Hydrogen Storage in Metal-Containing Inorganic Nanostructures and Related Materials. *Adv. Mater.* **2004**, *16*, 765–777.

(26) Leela Mohana Reddy, A.; Tanur, A. E.; Walker, G. C. Synthesis and Hydrogen Storage Properties of Different Types of Boron Nitride Nanostructures. *Int. J. Hydrogen Energy* **2010**, *35*, 4138–4143.

(27) Rowsell, J. L. C.; Yaghi, O. M. Strategies for Hydrogen Storage in Metal-Organic Frameworks. *Angew. Chem. Int. Ed.* **2005**, *44*, 4670–4679.

(28) Murray, Leslie J and Dinca, Mircea and Long, J. R. Hydrogen Storage in Metal-Organic Frameworks. *Chem. Soc. Rev.* **2009**, *38*, 1294--1314.

(29) Tylianakis, E.; Klontzas, E.; Froudakis, G. E. Multi-Scale Theoretical Investigation of Hydrogen Storage in Covalent Organic Frameworks. *Nanoscale* **2011**, *3*, 856–869.

(30) Germain, J.; Fréchet, J. M. J.; Svec, F. Nanoporous Polymers for Hydrogen Storage. *Small* **2009**, *5*, 1098–1111.

(31) McKeown, N. B.; Budd, P. M. Polymers of Intrinsic Microporosity (PIMs): Organic Materials for Membrane Separations, Heterogeneous Catalysis and Hydrogen Storage. *Chem. Soc. Rev.* **2006**, *35*, 675–683.

(32) Li, W.; Li, C.; Ma, H.; Chen, J. Magnesium Nanowires: Enhanced Kinetics for Hydrogen Absorption and Desorption. *J. Am. Chem. Soc.* **2007**, *129*, 6710–6711.

(33) Xie, L.; Zheng, J.; Liu, Y.; Li, Y.; Li, X. Synthesis of Li_2NH Hollow Nanospheres with Superior Hydrogen Storage Kinetics by Plasma Metal Reaction. *Chem. Mater.* **2008**, *20*, 282–286.

(34) Filinchuk, Y.; Richter, B.; Jensen, T. R.; Dmitriev, V.; Chernyshov, D.; Hagemann, H. Porous and Dense Magnesium Borohydride Frameworks: Synthesis, Stability, and

Reversible Absorption of Guest Species. *Angew. Chem. Int. Ed.* **2011**, *123*, 11358–11362.

(35) Li, G.; Kobayashi, H.; Taylor, J. M.; Ikeda, R.; Kubota, Y.; Kato, K.; Takata, M.; Yamamoto, T.; Toh, S.; Matsumura, S.; Kitagawa, H. Hydrogen Storage in Pd Nanocrystals Covered with a Metal-Organic Framework. *Nat. Mater.* **2014**, *13*, 802–806.

(36) Konarova, M.; Tanksale, A.; Beltramini, J. N.; Lu, G. Q. Porous MgH_2/C Composite with Fast Hydrogen Storage Kinetics. *Int. J. Hydrogen Energy* **2012**, *37*, 8370–8378.

(37) Zheng, S.; Fang, F.; Zhou, G.; Chen, G.; Ouyang, L.; Zhu, M.; Sun, D. Hydrogen Storage Properties of Space-Confined $NaAlH_4$ Nanoparticles in Ordered Mesoporous Silica. *Chem. Mater.* **2008**, *20*, 3954–3958.

(38) Xia, G.; Tan, Y.; Chen, X.; Sun, D.; Guo, Z.; Liu, H.; Ouyang, L.; Zhu, M.; Yu, X. Monodisperse Magnesium Hydride Nanoparticles Uniformly Self-Assembled on Graphene. *Adv. Mater.* **2015**, *27*, 5981–5988.

(39) Xia, G.; Li, D.; Chen, X.; Tan, Y.; Tang, Z.; Guo, Z.; Liu, H.; Liu, Z.; Yu, X. Carbon-Coated Li_3N Nanofibers for Advanced Hydrogen Storage. *Adv. Mater.* **2013**, *25*, 6238–6244.

(40) Lim, D. W.; Yoon, J. W.; Ryu, K. Y.; Suh, M. P. Magnesium Nanocrystals Embedded in a Metal-Organic Framework: Hybrid Hydrogen Storage with Synergistic Effect on Physi- and Chemisorption. *Angew. Chem. Int. Ed.* **2012**, *51*, 9814–9817.

(41) Klebanoff, L.E. and Keller, J.O., 5 Years of Hydrogen Storage Research in the U.S. DOE Metal Hydride Center of Excellence (MHCoE), *Int. J. Hydrogen Energy,* **2013**, *38*, 4533-4576.

(42) Pasini, J. M.; Corgnale, C.; Van Hassel, B. A.; Motyka, T.; Kumar, S.; Simmons, K. L. Metal Hydride Material Requirements for Automotive Hydrogen Storage Systems. *Int. J. Hydrogen Energy* **2013**, *38*, 9755–9765.

(43) Ray, K. G.; Klebanoff, L. E.; Lee, J. R. I.; Stavila, V.; Heo, T. W.; Shea, P.; Baker, A. A.; Kang, S.; Bagge-Hansen, M.; Liu, Y. S.; White, J. L.; Wood, B. C. Elucidating the Mechanism of MgB_2 Initial Hydrogenation via a Combined Experimental-Theoretical Study. *Phys. Chem. Chem. Phys.* **2017**, *19*, 22646–22658.

(44) Konoplev, V. N.; Bakulina, V. M. Some Properties of Magnesium Borohydride. *Bull. Acad. Sci. USSR Div. Chem. Sci.* **1971**, *20*, 136–138.

(45) Nakamori, Y.; Miwa, K.; Ninomiya, A.; Li, H.; Ohba, N.; Towata, S. I.; Züttel, A.; Orimo, S. I. Correlation between Thermodynamical Stabilities of Metal Borohydrides and Cation Electronegativites: First-Principles Calculations and Experiments. *Phys. Rev. B - Condens. Matter Mater. Phys.* **2006**, *74*, 045126.

(46) Chłopek, K.; Frommen, C.; Léon, A.; Zabara, O.; Fichtner, M. Synthesis and Properties of Magnesium Tetrahydroborate, $Mg(BH_4)_2$. *J. Mater. Chem.* **2007**, *17*, 3496–3503.

(47) Soloveichik, G. L.; Gao, Y.; Rijssenbeek, J.; Andrus, M.; Kniajanski, S.; Bowman, R. C.; Hwang, S. J.; Zhao, J. C. Magnesium Borohydride as a Hydrogen Storage Material: Properties and Dehydrogenation Pathway of Unsolvated $Mg(BH_4)_2$. *Int. J. Hydrogen Energy*, **2009**, *34*, 916–928.

(48) Li, H. W.; Miwa, K.; Ohba, N.; Fujita, T.; Sato, T.; Yan, Y.; Towata, S.; Chen, M. W.; Orimo, S. Formation of an Intermediate Compound with a $B_{12}H_{12}$ Cluster: Experimental and Theoretical Studies on Magnesium Borohydride $Mg(BH_4)_2$. *Nanotechnology* **2009**, *20*, 204013.

(49) Yang, J.; Zhang, X.; Zheng, J.; Song, P.; Li, X. Decomposition Pathway of $Mg(BH_4)_2$ under Pressure: Metastable Phases and Thermodynamic Parameters. *Scr. Mater.* **2011**, *64*, 225–228.

(50) Chong, M.; Karkamkar, A.; Autrey, T.; Orimo, S.; Jalisatgi, S.; Jensen, C. M. Reversible Dehydrogenation of Magnesium Borohydride to Magnesium Triborane in the Solid State under Moderate Conditions. *Chem. Commun.* **2011**, *47*, 1330–1332.

(51) Chong, M.; Matsuo, M.; Orimo, S. I.; Autrey, T.; Jensen, C. M. Selective Reversible Hydrogenation of $Mg(B_3H_8)_2/MgH_2$ to $Mg(BH_4)_2$: Pathway to Reversible Borane-Based Hydrogen Storage? *Inorg. Chem.* **2015**, *54*, 4120–4125.

(52) Zavorotynska, O.; Deledda, S.; Hauback, B. C. Kinetics Studies of the Reversible Partial Decomposition Reaction in $Mg(BH_4)_2$. *Int. J. Hydrogen Energy* **2016**, *41*, 9885–9892.

(53) Zhang, Y.; Majzoub, E.; Ozoliņš, V.; Wolverton, C. Theoretical Prediction of Metastable

Intermediates in the Decomposition of $Mg(BH_4)_2$. *J. Phys. Chem. C* **2012**, *116*, 10522–10528.

(54) Severa, G.; Rönnebro, E.; Jensen, C. M. Direct Hydrogenation of Magnesium Boride to Magnesium Borohydride: Demonstration of >11 Weight Percent Reversible Hydrogen Storage. *Chem. Commun.* **2010**, *46*, 421–423.

(55) Pistidda, C.; Garroni, S.; Dolci, F.; Bardají, E. G.; Khandelwal, A.; Nolis, P.; Dornheim, M.; Gosalawit, R.; Jensen, T.; Cerenius, Y.; Suriñach, S.; Baró, M. D.; Lohstroh, W.; Fichtner, M. Synthesis of Amorphous $Mg(BH_4)_2$ from MgB_2 and H_2 at Room Temperature. *J. Alloys Compd.* **2010**, *508*, 212–215.

(56) Newhouse, R. J.; Stavila, V.; Hwang, S. J.; Klebanoff, L. E.; Zhang, J. Z. Reversibility and Improved Hydrogen Release of Magnesium Borohydride. *J. Phys. Chem. C* **2010**, *114*, 5224–5232.

(57) Li, H. W.; Matsunaga, T.; Yan, Y.; Maekawa, H.; Ishikiriyama, M.; Orimo, S. I. Nanostructure-Induced Hydrogenation of Layered Compound MgB_2. *J. Alloys Compd.* **2010**, *505*, 654–656.

(58) Liu, Y.-S.; Ray, K. G.; Jørgensen, M.; Mattox, T. M.; Cowgill, D. F.; Eshelman, H.; Sawvel, A. M.; Snider, J. L.; York, W.; Wijeratne, P.; Pham, A.; Gunda, H.; Li, S.; Heo, T. W.; Kang, S.; Jensen, T. R.; Stavila, V.; Wood, B. C.; Klebanoff, L. E. Nanoscale Mg-B Via Surfactant Ball Milling of MgB_2: Morphology, Composition and Improved Hydrogen Storage Properties. *J. Phys. Chem. C* **2020**, *124*, 21761–21771.

(59) Gunda, H.; Das, S. K.; Jasuja, K. Simple, Green, and High-Yield Production of Boron-Based Nanostructures with Diverse Morphologies by Dissolution and Recrystallization of Layered Magnesium Diboride Crystals in Water. *ChemPhysChem* **2018**, *19*, 880–891.

(60) Das, S. K.; Bedar, A.; Kannan, A.; Jasuja, K. Aqueous Dispersions of Few-Layer-Thick Chemically Modified Magnesium Diboride Nanosheets by Ultrasonication Assisted Exfoliation. *Sci. Rep.* **2015**, *5*, 10522.

(61) James, A. L.; Jasuja, K. Chelation Assisted Exfoliation of Layered Borides towards Synthesizing Boron Based Nanosheets. *RSC Adv.* **2017**, *7*, 1905–1914.

(62) Ratnam, D.; Das, S. K.; Jasuja, K. Ionic Liquid Assisted Exfoliation of Layered Magnesium Diboride. *IOP Conf. Ser. Mater. Sci. Eng.* **2017**, *225*, 12111.

(63) Das, S. K.; Jasuja, K. Chemical Exfoliation of Layered Magnesium Diboride To Yield Functionalized Nanosheets and Nanoaccordions for Potential Flame Retardant Applications. *ACS Appl. Nano Mater.* **2018**, *1*, 1612–1622.

(64) Saraswat, R.; James, A. L.; Jasuja, K. High Yield Synthesis of Boron-Based Nanosheets. *Adv. Appl. Ceram.* **2019**, *118* (4), 209–216.

(65) James, A.L.; Khandelwal, S.; Dutta, A.; Jasuga, K.; Boron -based Nanosheets as Reducing Templates in Aqueous Solutions: Towards Novel Nanohybrids with Gold Nanoparticles in Graphene. *Nanoscale* **2018**, *10*, 20514-20518.

(66) Gunda, H.; Ghoroi, C.; Jasuja, K. Layered Magnesium Diboride and Its Derivatives as Potential Catalytic and Energetic Additives for Tuning the Exothermicity of Ammonium Perchlorate. *Thermochim. Acta* **2020**, *690*, 178674.

(67) For an example of the use of the Debye-Scherrer equation, see: Deshmukh, S. B.; Bari, R. H.; Patil, G. E.; Kajale, D. D.; Jain, G. H.; Patil, L. A. Preparation and Characterization of Zirconia Based Thick Film Resistor as a Ammonia Gas Sensor. *Int. J. Smart Sens. Intell. Syst.* **2012**, *5*, 540–558.

(68) Kresse, G.; Hafner, J. Ab Initio Molecular Dynamics for Liquid Metals. *Phys. Rev. B: Condens. Matter Mater. Phys*. **1993**, *47*, 558−561.

(69) Kresse, G.; Hafner, J. Ab Initio Molecular-Dynamics Simulation of the Liquid-Metalamorphous-Semiconductor Transition in Germanium. *Phys. Rev. B: Condens. Matter Mater. Phys*. **1994**, *49*, 14251−14269.

(70) Kresse, G.; Furthmüller, J. Efficient Iterative Schemes for Ab Initio Total-Energy Calculations Using a Plane-Wave Basis Set. *Phys. Rev. B: Condens. Matter Mater. Phys*. **1996**, *54*, 11169−11186.

(71) Kresse, G.; Joubert, D. From Ultrasoft Pseudopotentials to the Projector Augmented-Wave Method. *Phys. Rev. B: Condens. Matter Mater. Phys.* **1999**, *59*, 1758−1775.

(72) Perdew, J. P.; Burke, K. Comparison Shopping for a Gradient Corrected Density Functional.*Int. J. Quantum Chem*. **1996**, *57*, 309– 319.

(73) Holder, C. F.; Schaak, R. E. Tutorial on Powder X-Ray Diffraction for Characterizing Nanoscale Materials. *ACS Nano*, **2019**, *13*, 7359–7365.

(74) Kim, S.-E.; Shon, I.-J. The Effect of Ball Milling on Properties and Sintering of Nanostructured TiB_2. *J. Nanosci. Nanotechnol.* **2021**, *21*, 3934–3937.

(75) Kim, S.-E.; Yoon, J.-K.; Shon, I.-J. Mechanochemical Synthesis and Rapid Consolidation of Nanostructured Nb–ZrO_2 Composite. *J. Nanosci. Nanotechnol.* **2020**, *20*, 4253–4256.

(76) Zhang, L.; Huang, Z.; Liu, Y.; Shen, Y.; Li, K.; Cao, Z.; Ren, Z.; Jian, Y. Effects of Mechanical Ball Milling Time on the Microstructure and Mechanical Properties of Mo_2NiB_2-Ni Cermets. *Materials,* **2019**, *12*, 1926-1932.

(77) Park, N.-R.; Cho, W.-J.; Kim, S.-E.; Shon, I.-J. The Effect of Ball Milling on Properties and Consolidation of Nanostructured ZrB_2. *J. Nanosci. Nanotechnol.* **2018**, *19*, 2295–2297.

(78) Kim, S.-E.; Shon, I.-J. The Effect of Ball Milling on Properties and Sintering of Nanostructured TiB_2. *J. Nanosci. Nanotechnol.* **2021**, *21*, 3934–3937.

(79) Liu, Y.-S.; Klebanoff, L.E.; Wijeratne, P.; Cowgill, D.F.; Stavila, V.; Heo, T.W.; Wood, B. C. Investigating Possible Kinetic Limitations to MgB_2 Hydrogenation, *Int. J. Hydrogen Energy*, **2019**, *44*, 31239 - 31256.

(80) Snider, J.L., Liu, Y.-S., Sawvel, A.M., Wan, L.F., Stavila, V., Mattox, T.M.;; Klebanoff, L.E. "The Influence of LiH and TiH_2 on Hydrogen Storage in MgB_2 I: Promotion of Bulk Hydrogenation at Reduced Temperature," *Int. J. Hydrogen Energy*, **2022**, *47*, 387 – 402.

(81) Snider, J.L.; Mattox, T.M.; Liu, Y.-S.; Wan, L.F.; Wijeratne, P.; Allendorf, M.D.; Stavila, V.; Klebanoff, L.E. The Influence of LiH and TiH_2 on Hydrogen Storage in MgB_2 II: XPS Study of Surface and Near-surface Phenomena, *Int. J. Hydrogen Energy*, **2022**, *47*, 403 – 419.

(82) Parviz, D.; Irin, F.; Shah, S. A.; Das, S.; Sweeney, C. B.; Green, M. J. Challenges in Liquid-Phase Exfoliation, Processing, and Assembly of Pristine Graphene. *Adv. Mater.* **2016**, *28*, 8796-8818 .

(83) Cheng, C.; Li, D. Solvated Graphenes: An Emerging Class of Functional Soft Materials. *Adv. Mater.* **2013**, *25*, 13–30.

(84) Landau, M. V.; Vidruk, R.; Vingurt, D.; Fuks, D.; Herskowitz, M. Grain Boundaries in Nanocrystalline Catalytic Materials as a Source of Surface Chemical Functionality. *Rev. Chem. Eng.* **2014**, *30*, 379–401.

(85) Zavorotynska, O.; El-Kharbachi, A.; Deledda, S.; Hauback, B. C. Recent Progress in Magnesium Borohydride $Mg(BH_4)_2$: Fundamentals and Applications for Energy Storage. *Int. J. Hydrogen Energy,* **2016**, *41*, 14387–14403.

(86) Chłopek, K.; Frommen, C.; Léon, A.; Zabara, O.; Fichtner, M. Synthesis and Properties of Magnesium Tetrahydroborate, $Mg(BH_4)_2$. *J. Mater. Chem.* **2007**, *17*, 3496–3503.

(87) Remhof, A.; Yan, Y.; Rentsch, D.; Borgschulte, A.; Jensen, C. M.; Züttel, A. Solvent-Free Synthesis and Stability of $MgB_{12}H_{12}$. *J. Mater. Chem. A* **2014**, *2*, 7244-7251.

(88) Sethio, D.; Lawson Daku, L. M.; Hagemann, H. A Theoretical Study of the Spectroscopic Properties of B_2H_6 and of a Series of B_xHy^{z-} Species (x = 1-12, y = 3-14, z = 0-2): From BH_3 to $B_{12}H_{12}^{2-}$. *Int. J. Hydrogen Energy*, **2016**, *41*, 6814–6824.

(89) Yan, Y.; Li, H. W.; Maekawa, H.; Aoki, M.; Noritake, T.; Matsumoto, M.; Miwa, K.; Towata, S. I.; Orimo, S. I. Formation Process of $[Bi_2H_{12}]^{2-}$ from $[BH_4]^-$ during the Dehydrogenation Reaction of $Mg(BH_4)_2$. *Mater. Trans.* **2011**, *52*, 1443–1446.

(90) Wang, Y.; Michel, K.; Zhang, Y.; Wolverton, C. Thermodynamic stability of transi- tion metals on the Mg-terminated MgB_2 (0001) surface and their effects on hydrogen dissociation and diffusion. *Phys. Rev. B* **2015**, *91*, 155431.

(91) Li, S.; Gunda, H.; Ray, K.; Wong, C.-S.; Xiao, P.; Friddle, R.; Liu, Y.-S.; Kang, S.; Sugar, J.; Kolasinski, R., et al. Spontaneous Dynamical Disordering of Borophenes in MgB_2 and Related Metal Borides. *Nat. Commun.*, **2021**, *12*, 6268.

(92) Ray, K. G.; Klebanoff, L. E.; Stavila, V.; Kang, S.; Wan, L. F.; Li, S.; Heo, T. W.; Allendorf, M. D.; Lee, J. R. I.; Baker, A. A.; Wood, B. C. Understanding Hydrogenation Chemistry at MgB_2 Reactive Edges from *Ab Initio* Molecular Dynamics. *ACS Appl. Mater. Interfaces* **2022**, *14*, 20430-20442.

(93) Patidar, R.; Gunda, H.; Varma, A. K.; Gawas, R.; Das, S. K.; Jasuja, K. Co-Solvent Exfoliation of Layered Titanium Diboride into Few-Layer-Thick Nanosheets. *Ceram. Int.* **2020**, *46*, 28324−28331.

(94) James, A. L.; Lenka, M.; Pandey, N.; Ojha, A.; Kumar, A.; Saraswat, R.; Thareja, P.; Krishnan, V.; Jasuja, K. Processable Dispersions of Photocatalytically Active Nanosheets Derived from Titanium Diboride: Self Assembly into Hydrogels and Paper-like Macrostructures. *Nanoscale* **2020**, *12*, 17121−17131.

(95) Gunda, H.; Klebanoff, L. E.; Sharma, P. A.; Varma, A. K.; Dolia, V.; Jasuja, K.; Stavila, V. Progress, Challenges, and Opportunities in the Synthesis, Characterization, and Application of Metal-Boride-Derived Two-Dimensional Nanostructures. *ACS Mater. Lett.* **2021**, 535–556.

TOC Figure

Hydrogen Storage Properties of Magnesium Diboride Nanosheets Synthesized via Mechanochemical Exfoliation